RSC Advances

PAPER

View Article Online
View Journal | View Issue

Cite this: RSC Adv., 2025, 15, 42981

# Determination of the light matter interaction and thermal heat conversion efficiency of $K_2TlAsZ_6$ (Z = F, Cl, Br, and I) using a DFT approach

Murtaza Shahab,†[a] Muhammad Awais Jehangir,†[d] Muhammad Noman,[a] Saad Alshammari,*[b] Arafa A. Yagob[c] and G. Murtaza *[a]

Double perovskites have garnered significant attention as promising alternatives for sustainable energy solutions owing to their structural versatility and potential for integration into optoelectronic technologies. Halide double perovskites $K_2TlAsZ_6$ (Z = F, Cl, Br, and I) were systematically studied using density functional theory to assess their potential for optoelectronic and thermoelectric applications. Calculations were performed using the FP-LAPW + lo method, confirming structural and thermodynamic stability *via* formation energy, and the Goldschmidt's tolerance factor. The electronic structure calculations using the TB-mBJ + SOC potential revealed direct bandgaps ranging from 3.25 eV (Z = F) to 0.37 eV (Z = I), with significant UV absorption observed in the optical spectra. Thermoelectric performance *versus* chemical potential, evaluated *via* the Boltzmann transport theory, showed promising *ZT* values approaching 1.0 at 1000 K. Additionally, negative Gibbs free energy and increasing entropy with temperature indicate good thermal stability. These results suggest that $K_2TlAsZ_6$ compounds are promising materials for next-generation optoelectronic and thermoelectric devices.

Received 12th August 2025
Accepted 20th October 2025

DOI: 10.1039/d5ra05932a

rsc.li/rsc-advances

## 1 Introduction

Perovskite-based materials have attracted extensive attention in recent years due to their diverse physicochemical properties and applicability in photocatalysis, optoelectronics, thermoelectric, and spintronics.[1,2] Lead-based halide perovskites have achieved power conversion efficiencies above 25%, surpassing thin-film silicon and copper indium gallium selenide solar cells.[3] Nevertheless, environmental concerns regarding lead toxicity have driven the search for non-toxic alternatives, leading to the development of lead-free double perovskite halides with competitive optoelectronic performance.[4]

Halide perovskites crystallize in the $ABX_3$ form, while double perovskites adopt $A_2BB'X_6$, where A is a monovalent cation, B and B′ are metal cations of different oxidation states, and X is a halide anion.[5] Lead-free double perovskites (DPs) display distinctive electronic and optical characteristics, making them promising for renewable energy applications.[6] For instance, $Rb_2AgAsX_6$ (X = Br, I, and Cl) shows tunable band gaps *via* halide substitution,[7] and $Cs_2ScTlX_6$ (X = Cl, Br, and I) exhibits mechanical stability in cubic symmetry as confirmed by elastic constants and tolerance factors.[8] $Cs_2LiYCl_6$, synthesized for thermal neutron detection, demonstrates potential as a scintillator material.[9] Computational investigations reveal favorable optoelectronic behavior in $Rb_2AgBiI_6$,[10] while $X_2AgBiI_6$ (X = Cs, K, and Rb) offers high thermoelectric figures of merit with advantageous optical properties.[11] $Cs_2SnI_6$ has been examined as a lead-free absorber for solar applications,[12] and $Cs_2BiAgX_6$ (X = Br and Cl) prepared *via* solid-solution synthesis exhibits direct band-gap behavior with modified transport characteristics.[13]

Within this class, potassium-based perovskites are emerging as particularly promising due to their stability and favorable electromagnetic, thermoelectric, and optoelectronic properties.[14] Potassium doping has enabled the fabrication of hysteresis-free solar cells,[15] while high-efficiency, low-hysteresis devices have been reported using potassium-based perovskites.[16] Additionally, potassium thiocyanate interlayers have been proposed for eco-friendly indoor and outdoor photovoltaics.[17] These findings underscore the potential of K-based halides for large-scale deployment in sustainable energy technologies,[18] motivating continued research into novel potassium-based perovskite compositions for advanced solar energy conversion and storage applications.

Munir *et al.* (2025) have thoroughly examined the structural, electronic, mechanical, optical, and thermoelectric properties

---

[a] Materials Modeling Lab, Department of Physics, Islamia College Peshawar, Pakistan. E-mail: murtaza@icp.edu.pk

[b] Department of Mechanical and Industrial Engineering, College of Engineering, Majmaah University, Al Majmaah 11952, Saudi Arabia

[c] Department of Physical Sciences, Physics Division, College of Science, Jazan University, P. O. Box 114, 45142, Jazan, Saudi Arabia

[d] Institute of Fundamental and Frontier Sciences, University of Electronic Science and Technology of China, Chengdu, Sichuan 611731, China

† Murtaza Shahab and Muhammad Awais Jehangir made equal contributions.

of $K_2TlAsX_6$ ($X = Cl$ and Br) double perovskites, employing first-principles calculations within the framework of density functional theory (DFT). The electronic band structure was computed using the mBJ exchange potential, both with and without the inclusion of spin orbit coupling (SOC) effects, to account for relativistic interactions. Structural stability was confirmed through negative formation energies, optimized lattice parameters, positive phonon frequencies, and tolerance and octahedral factors within the permissible range for stable perovskite formation. Elastic constants were determined and the associated mechanical parameters, including elastic anisotropy, Pugh's ratio, Poisson's ratio, and Cauchy pressure, were derived to assess the ductility and mechanical anisotropy. Both compounds exhibit direct band gaps, with $K_2TlAsCl_6$ showing gaps of 2.22 eV (modified Becke–Johnson, mBJ) and 1.59 eV (mBJ + SOC), while $K_2TlAsBr_6$ presents gaps of 1.97 eV and 1.51 eV, respectively. The optical properties reveal strong absorption in the visible and ultraviolet regions, suggesting potential for optoelectronic integration. Moreover, electronic transport analysis indicates high electrical conductivity, favorable thermoelectric figure of merit ($ZT$) and low lattice thermal conductivity, making these halide perovskites promising candidates for energy-efficient and green optoelectronic applications.[19] Although $K_2TlAsZ_6$ are designed as lead-free alternatives, it should be noted that these systems contain thallium (Tl) and arsenic (As), both of which are toxic and pose environmental and health risks if improperly handled. Therefore, the term "*lead-free*" in this context refers specifically to the absence of lead, a well-known hazardous element in conventional perovskites, rather than indicating complete non-toxicity.

The aim of the present work is to assess the structural, optoelectronic, thermoelectric, and thermodynamic properties of $K_2TlAsZ_6$ ($Z = F$, Cl, Br, and I). Our findings are intended to support further theoretical and practical studies of $K_2TlAsZ_6$ ($Z = F$, Cl, Br, and I) halide double perovskites, with an emphasis on their possible applications in thermoelectric and optoelectronic devices.

## 2 Methods of simulations

Utilizing the WIEN2K algorithm,[20] a density functional theory (DFT) method based on the FP-APW + lo methodology was used to study the optoelectronic and transport characteristics of $K_2TlAsZ_6$ ($Z = F$, Cl, Br, and I). PBEsol-GGA, a generalized gradient approximation, was used in particular to optimize the structural parameters.[21] To assess the structural and dynamic stability of the compounds being studied, we computed the Goldschmidt tolerance factor, also known as the enthalpy of formation. We used PBEsol-GGA, in combination with the Trans and Blaha modified Becke–Johnson techniques (TB-mBJ), along with the SOC to precisely determine the required band gaps.[22] The electrical system's solution is regarded as spherically harmonic inside the muffin-tin sphere, but it exhibits plane wave-like behavior in the interstitial area. The initial parameters evaluated were the Gaussian parameter $G_{\max} = 16$, the product of the wave vector and muffin radius $K_{\max} \times R_{MT} = 8$, and the angular momentum $I = 10$ in the reciprocal lattice. In a $k$-mesh of order $10 \times 10 \times 10$, the correctness of the convergence criterion was tested using the 1000 $k$-point, where the energy emitted from the system remains constant.[23] At 0.01 mRy, charge convergence is attained. Furthermore, we used the convergent energy and optimum electronic structures using the TB-mBJ method to calculate the optical and photovoltaic characteristics. The BoltzTraP algorithm[24] with the combination of DFT and semiclassical transport theory is implemented in WIEN2k to compute the electronic transport coefficients of the studied compounds.

## 3 Results and discussion

### 3.1 Stability criteria for $K_2TlAsZ_6$ ($Z = F$, Cl, Br, and I)

To assess a structure's stability, we can compute Goldsmith's tolerance factor using the formula:[25]

$$T_F = \frac{R_A + R_X}{\sqrt{2}\left(\left(\frac{R_B + R_{B'}}{2}\right) + R_X\right)} \qquad (1)$$

where $R_{(K)}$, $R_{Tl}$, $R_{As}$, and $R_{(F/Cl/Br/I)}$ are the Shannon ionic radii for the potassium, thallium, arsenic, and halide atoms, respectively, in this context. Under ideal conditions, Goldsmith's criteria for stable cubic perovskites often approaches unity. Subsequently, the range of $T_F$ values among 0.8 and 1.0 is decisive for stable cubic arrangements. As seen in Table 1, our calculated values fall within this steady range. Consequently, the halides under investigation exhibit stability in the cubic phase. $K_2TlAsF_6$ is at the optimum limit compared to $K_2TlAsCl_6$, $K_2TlAsBr_6$, and $K_2TlAsI_6$, according to a comparison analysis (see Fig. 1a). In order to show the materials' thermodynamic stability, the subsequent chemical expression is used to compute the formation enthalpy:

Table 1 Structural parameters and stability criteria for $K_2TlAsZ_6$ ($Z = F$, Cl, Br, and I)[a]

| Compounds | $K_2TlAsF_6$ | $K_2TlAsCl_6$ | $K_2TlAsBr_6$ | $K_2TlAsI_6$ |
|---|---|---|---|---|
| $a_0$ (Å) | 9.38 | 10.83<br>$11.00^A$ | 11.31<br>$11.53^A$ | 12.04 |
| $V_0$ [a.u.]$^3$ | 1394.21 | 2144.88<br>$2586.71^A$ | 2443.12<br>$2588.00^A$ | 2945.71 |
| $B$ (GPa) | 43.48 | 26.96<br>$24.00^A$ | 23.51<br>$20.31^A$ | 19.09 |
| B' | 5.00 | 5.00<br>$4.86^A$ | 5.00<br>$4.83^A$ | 5.00 |
| $E_0$ [Ry.] | −48707.17 | −53021.15<br>$-53047.39^A$ | −78750.39<br>$-78789.00^A$ | −132884.23 |
| $\tau_F$ | 1.0 | 0.96<br>$0.88^A$ | 0.95<br>$0.87^A$ | 0.93 |
| $\Delta H_F$ (eV/atom) | −1.90 | −1.41<br>$-1.92^A$ | −1.10<br>$-1.61^A$ | −0.67 |
| $E_{Cohesive}$ | 1.90 | 1.41 | 1.10 | 0.67 |
| $\rho$ (g cm$^{-3}$) | 3.79 | 2.98 | 3.84 | 4.26 |

[a] Ref$^{A}$.[19]

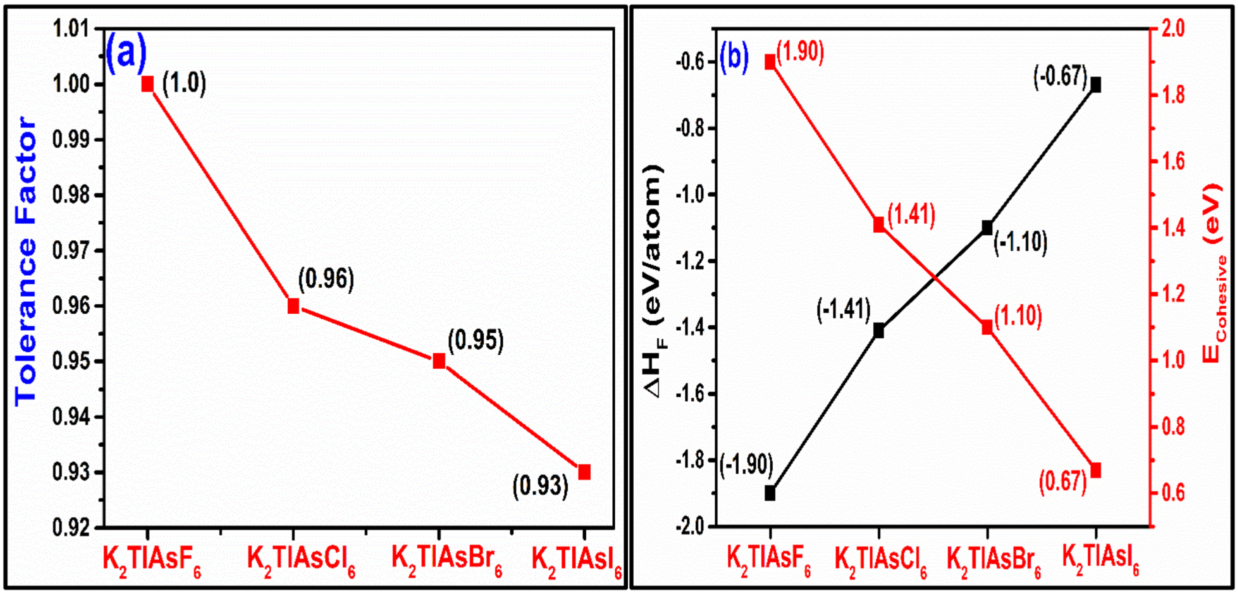

Fig. 1 (aand b) Tolerance factor ($T_F$), formation ($\Delta H_F$) and cohesive energies of $K_2TlAsZ_6$ (Z = F, Cl, Br, and I).

$$\Delta H_F = E_{(\mathrm{K})\mathrm{aTlbAsc}(\mathrm{F/Cl/Br/I})\mathrm{d}} - aE_{\mathrm{Kb}} - bE_{\mathrm{Tl}} - cE_{\mathrm{As}} - dE_{(\mathrm{F/Cl/Br/I})} \quad (2)$$

$$E_{\mathrm{Coh}} = [aE_{\mathrm{K}} + bE_{\mathrm{Tl}} + cE_{\mathrm{As}} + dE_{(\mathrm{F/Cl/Br/I})}] - E_{(\mathrm{K})_a\mathrm{Tl}_b\mathrm{As}_c(\mathrm{F/Cl/Br/I})_d} \quad (3)$$

where $E_{\mathrm{K}}$, $E_{\mathrm{Tl}}$, $E_{\mathrm{As}}$ and $E_{(\mathrm{F/Cl/Br/I})}$ signify the energies for the individual atoms K, Tl, As, and Z, respectively, and $E_{(\mathrm{K})_a\mathrm{Tl}_b\mathrm{As}_c(\mathrm{F/Cl/Br/I})_d}$ represents the total energy of the compounds under investigation. The conforming atoms is indicated by the subscripts *a*, *b*, *c*, and *d* in the equation above. Essentially, the negative value of $\Delta H_F$ indicates the amount of energy squandered throughout the material creation process. The materials' stability is essential. Table 1 displays the calculated values and shows the thermodynamic stabilities of the compounds under study.[1,26] The conclusions evidently indicate that $K_2TlAsF_6$ exhibits more stability than $K_2TlAsCl_6$, $K_2TlAsBr_6$, and $K_2TlAsI_6$ (see Fig. 1 (b)).

### 3.2 Structural properties

All calculations were conducted utilizing the crystal arrangements of $K_2TlAsZ_6$ (Z = F, Cl, Br, and I) halides, which are categorized within the space group $Fm\bar{3}m$#225 (see Fig. 2a). We utilized PBEsol-GGA to optimize halide DPs (see Fig. 2b–f) to determine the fundamental state lattice parameters, applying Birch Murnaghan's equation of states.[27] We determined the fundamental state lattice constant $a_0$ (Å) and bulk modulus *B* (GPa) by volume optimization, as demonstrated in the following Table 1. The values of $a_0$ show an upsurge from $K_2TlAsF_6$ to $K_2TlAsI_6$, which can be explained by the increase in atomic radii from F to I. The increase in distance between the atoms is a result of the larger cation size, which subsequently leads to a decrease in the density and strength of the compounds. Therefore, a drop in the bulk modulus $B_0$ is observed by substituting F with Cl, Br and I.[28]

### 3.3 Electronic properties

Using the modified Becke–Johnson (TB-mBJ) potential, the band structures of $K_2TlAsZ_6$ (Z = F, Cl, Br, and I) are illustrated in Fig. 3a–d. It was essential to use the mBJ + SOC method to get precise band gap metrics that corresponded to the empirically observed outcomes.[29] The band gap values were assessed for $K_2TlAsZ_6$ (Z = F, Cl, Br, and I) from 3.25 eV to 0.37 eV using mBJ + SOC methods as compared to the bandgap data of (2.22 eV) for $K_2TlAsCl_6$ and (1.97 eV) for $K_2TlAsBr_6$ reported by Junaid Munir *et al.* (2025).[19] With the valence band maximum (VBM) and conduction band minimum (CBM) located at the *Γ* high-symmetry point within the Brillouin zone, the compounds exhibit a direct band gap nature. Our findings suggest that these halides may find use in opto-electronic devices since their bandgap measurements lie within the IR to visible (VIS) and smaller UV spectrum range.

For evaluating the electronic characteristics of the compounds being studied, the TDOS and PDOS, utilizing TB-mBJ, are shown in Fig. 4a–d. The total contribution of each state is shown as TDOS throughout the occupied and unoccupied states, much like the band structure. The interband transitions and hybridization are entirely the result of the occupied state electrons, whose roles in the valence bands are seen in Fig. 4a–d. (F/Cl/Br/I)-5p makes the largest contribution, with As-3p making a smaller one in the semi-core regions of the occupied state, where electrons migrate to the unoccupied state. In the conduction band As-3p states make a larger contribution. The band gap values for $K_2TlAsZ_6$ (Z = F, Cl, Br, I) are determined in the range 3.25 eV to 0.37 eV using TB-mBJ methods. The investigated materials exhibit a direct band gap, with both the valence band maximum (VBM) and conduction band minimum (CBM) located at the *Γ* high-symmetry point in the Brillouin zone. These materials are therefore ideally suited for photovoltaic and optoelectronic

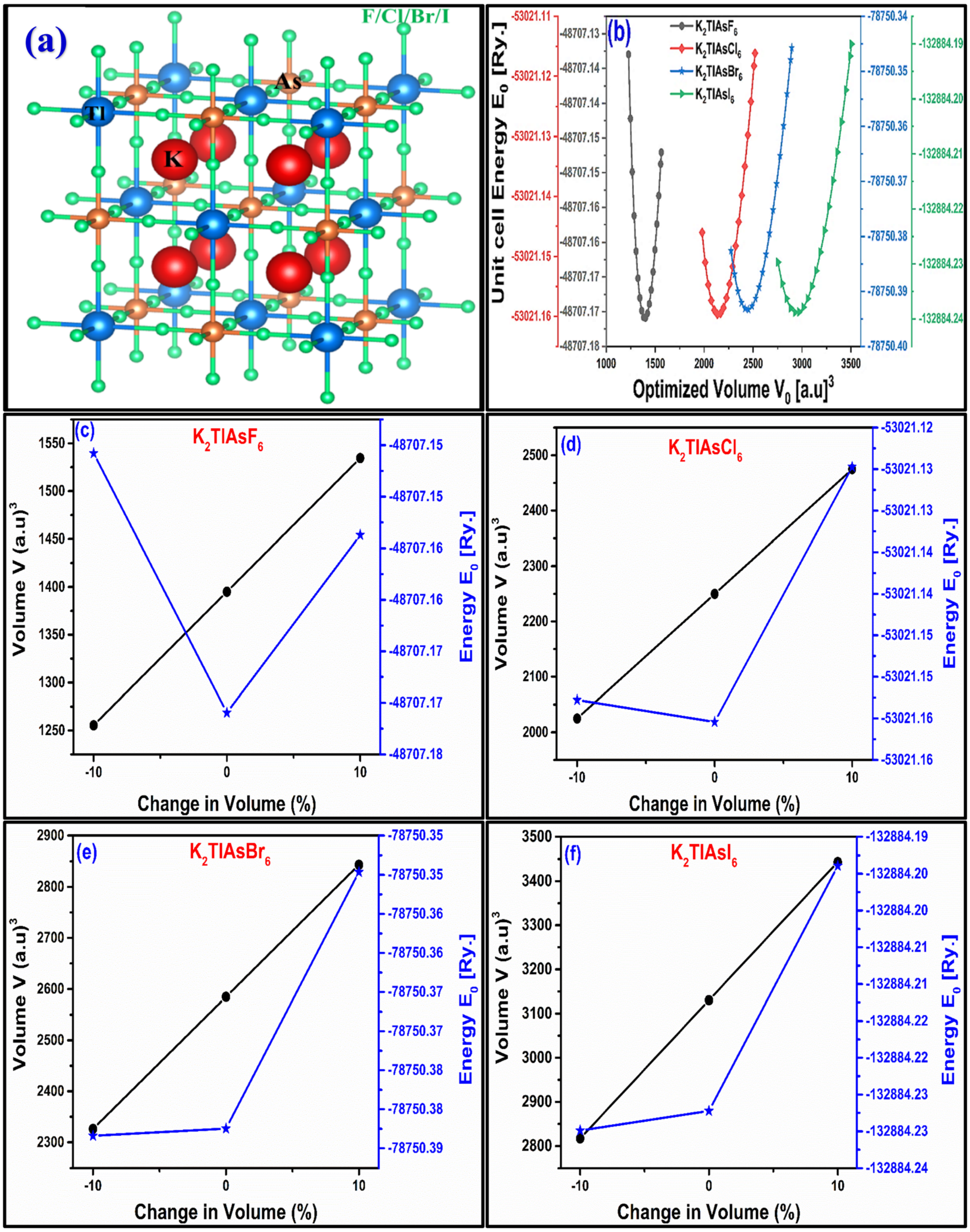

Fig. 2 (a–f) Crystal structure, $E$–$V$ parabolic curves, and unit cell volume and energy curves with percentage change in its volume for $K_2TlAsZ_6$ (Z = F, Cl, Br, and I).

applications, including tandem solar cells,[30] photodetectors that detect UV light,[31] sensors that detect infrared,[32] as well as LEDs.[33]

### 3.4 Optical properties

It is common practice to use the dispersion of both real and imaginary components of dielectric characteristics to derive crucial optical variables such as reflectivity $R(\omega)$ and refractive index $n(\omega)$, respectively. The absorption coefficient and optical conductivity can also be assessed using these metrics. The dielectric constant $\varepsilon(\omega)$, reflectivity $R(\omega)$, optical conductivity $\sigma(\omega)$, extinction coefficient $K(\omega)$, absorption coefficient $\alpha(\omega)$, refractive index $n(\omega)$, and other optical characteristics of $K_2TlAsZ_6$ (Z = F, Cl, Br, and I) were all calculated and presented using the TB-mBJ + SOC potential,[26] as revealed in Fig. 5a–h. Our halides crystallize in a cubic form; therefore, the mathematical expression that follows[34] from dispersion band theory (DBT) validates the close relationship between the band structures and the imaginary part of the dielectric tensor.

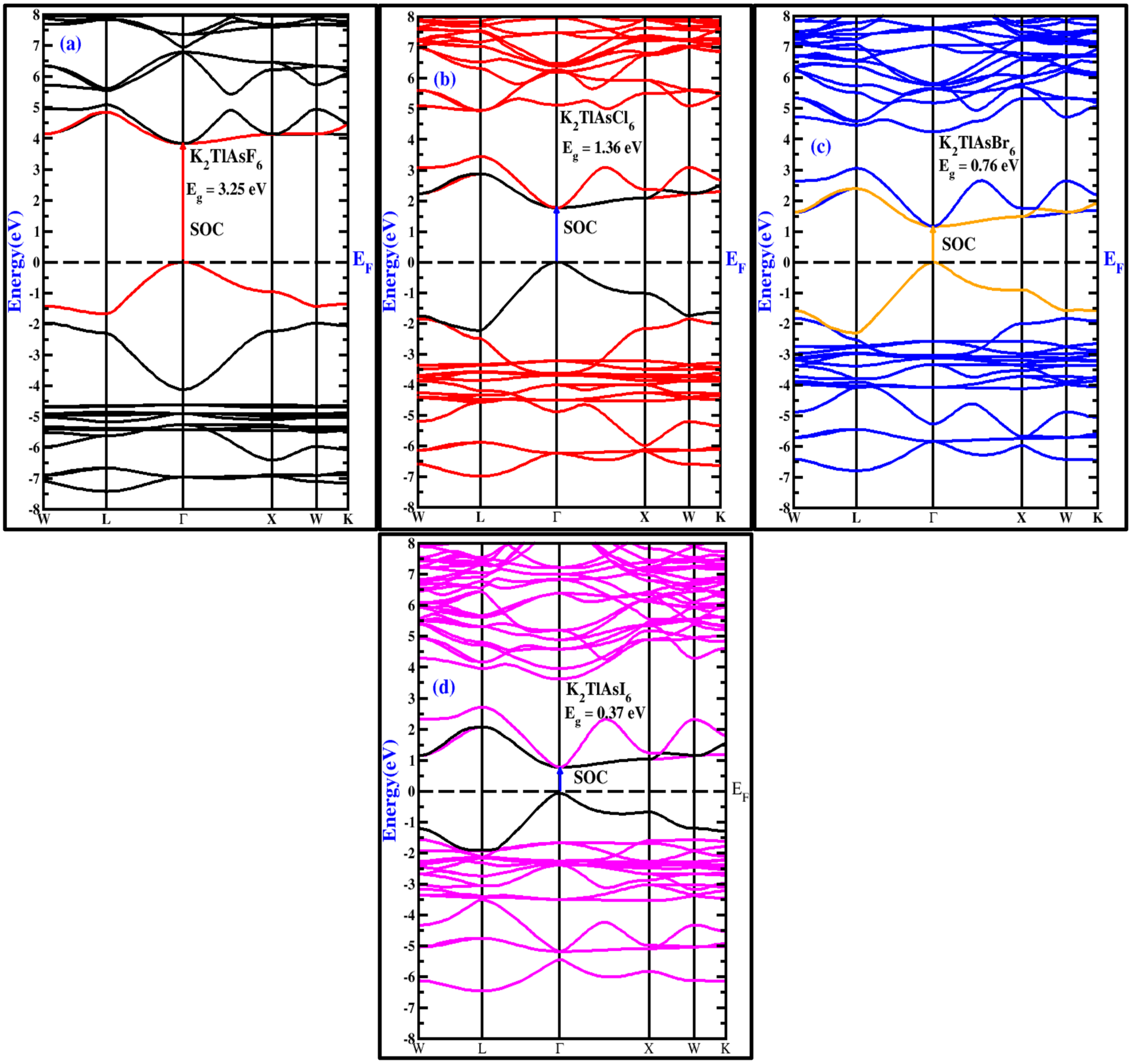

Fig. 3 (a–d) Band structure *via* mBJ + SOC for $K_2TlAsZ_6$ (Z = F, Cl, Br, and I).

$$\varepsilon_2(\omega) = \frac{e^2 h'}{\pi m^2 \omega^2} \sum_{v.c} \int |M_{cv}(k)|^2 \delta[\omega_{cv}(k) - \omega] d^3 k \qquad (4)$$

In this equation, $m$ is the mass, '$e$' is the electron's charge, and "$\omega$" is the electromagnetic radiation's angular frequency. Conversely, optical transitions are indicated by the dipole matrix element $M_{ck}(k) = \langle u_{ck}|e\nabla|\nu k\rangle$.[28] The real part of the dielectric function is found using the Kramers–Kronig equation, as explained in the next section:

$$\varepsilon_1(\omega) = 1 + \frac{2}{\pi} P \int_0^\infty \frac{\omega' \varepsilon_2(\omega')}{\omega'^2 - \omega^2} d\omega' \qquad (5)$$

The real component of the dielectric function is represented by $\varepsilon_1(\omega)$. The resonant frequencies for $K_2TlAsZ_6$ (Z = F, Cl, Br, and I) correspond to energy values ranging from 1.76 eV to 3.20 eV, where peak scattering of light occurs (Fig. 5a). The peaks exhibit a rapid decline to their lowest levels after achieving resonance. The zero-frequency limit of the real part of the dielectric function, $\varepsilon_1(0)$, which corresponds to the electronic contribution to the static dielectric constant, is a critical parameter in the optical spectrum. The calculated $\varepsilon_1(0)$ values for $K_2TlAsZ_6$ (Z = F, Cl, Br, and I) are summarized in Table 2.[35,36] An inverse dependence is observed between the band gap energy ($E_g$) and the static dielectric constant $\varepsilon_1(0)$. For the investigated $K_2TlAsZ_6$ (Z = F, Cl, Br, and I) compounds, $\varepsilon_1(0)$ exhibits an initial increase from zero frequency, attains a maximum, and then gradually decreases. With increasing

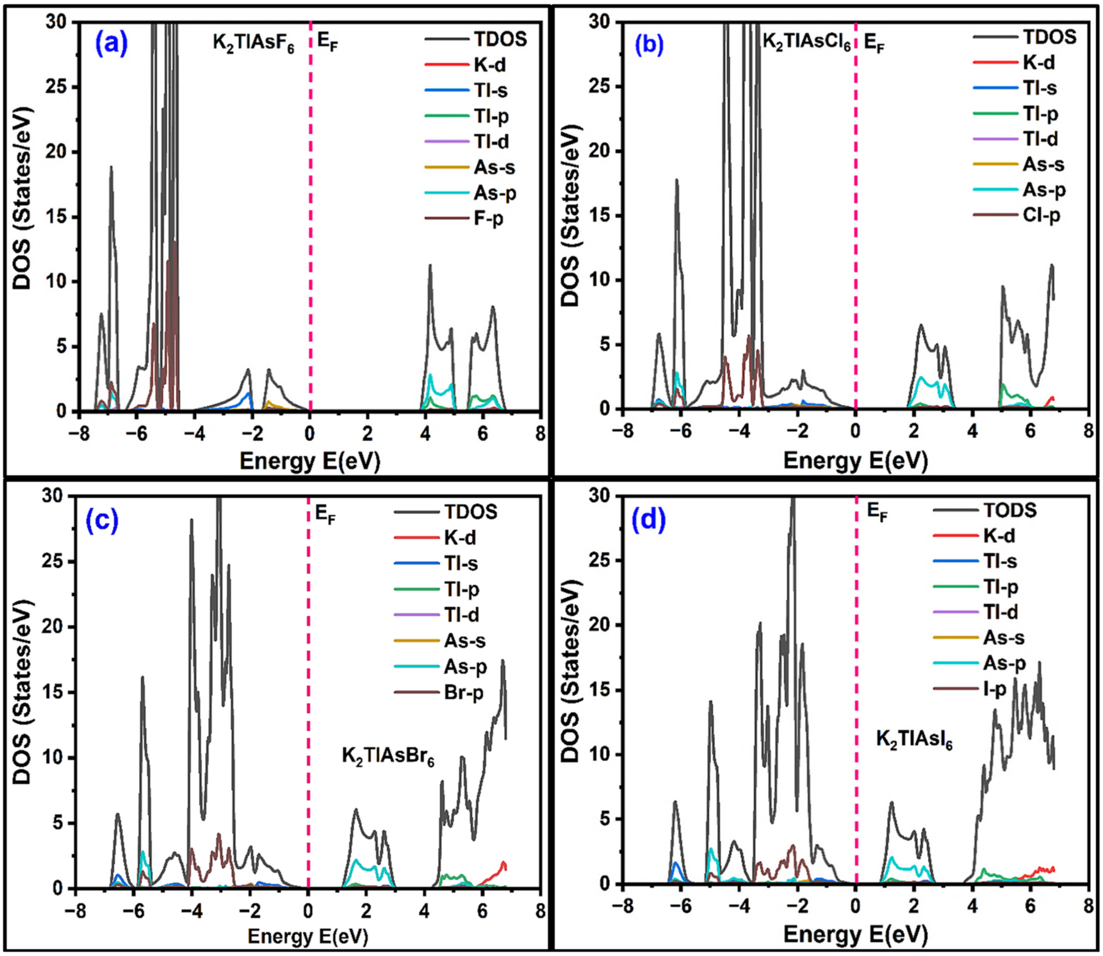

Fig. 4 (a–d) TDOS and PDOS using mBJ + SOC for $K_2TlAsZ_6$ (Z = F, Cl, Br, and I).

photon energy, additional distinct peaks emerge, as depicted in Fig. 5a. These spectral features, or kinks, are primarily located within the photon energy range of 1.76 eV to 3.20 eV. The maximum values of the real part of the dielectric function $\varepsilon_1(\omega)$ are found to be 3.22 at 4.93 eV for $K_2TlAsF_6$, 4.80 at 2.87 eV for $K_2TlAsCl_6$, 6.42 at 2.35 eV for $K_2TlAsBr_6$, and 9.90 at 1.72 eV for $K_2TlAsI_6$. The Penn model[32] has been employed to estimate $\varepsilon_1(0)$ and $E_g$, subject to the criterion for semiconducting materials, *i.e.*, $\varepsilon_1(0) > 1$.

$$\varepsilon_1(0) \approx 1 + \left(\frac{\hbar\omega_p}{E_g}\right) \tag{6}$$

The imaginary part of the dielectric function, $\varepsilon_2(0)$, is strongly influenced by the electronic band structure and plays a critical role in determining the optical absorption characteristics of the material. It provides insight into the interband electronic transitions. As the photon energy increases, transitions occur from the valence band, predominantly composed of halogen (F/Cl/Br/I)-5p orbitals, to the conduction band, which mainly consists of As-3p states. This transition consistently gives rise to the first prominent absorption peak observed across all investigated compounds. As illustrated in Fig. 5b, the second peak is also attributed to similar interband transitions. The calculated value of $\varepsilon_2(\omega)$ is determined from Fig. 5b, showing that all photons with energy $E$ (eV) beneath the matching energy gaps ($E_g$) of $K_2TlAsZ_6$ (Z = F, Cl, Br, and I) have a constant value of zero. The threshold points in the spectra of $\varepsilon_2(\omega)$ are 3.80 eV, 1.74 eV, 1.11 eV, and 0.67 eV for $K_2TlAsF_6$, $K_2TlAsCl_6$, $K_2TlAsBr_6$, and $K_2TlAsI_6$, respectively, as compared to the highest peak observed at 3.9 eV for $K_2TlAsCl_6$ and 3.1 eV for $K_2TlAsBr_6$.[19] A strong correlation is observed between the electronic band gaps and the corresponding peaks in the optical spectra. The calculated maximum values of the imaginary part of the dielectric function, $\varepsilon_2(\omega)$, for the $K_2TlAsZ_6$ (Z = F, Cl, Br, and I) compounds are 2.99 at 5.51 eV for $K_2TlAsF_6$, 3.73 at 3.30 eV for $K_2TlAsCl_6$, 5.07 at 3.14 eV for $K_2TlAsBr_6$, and 8.63 at 2.40 eV for $K_2TlAsI_6$. Notably, the most prominent absorption features appear near 3.1 eV and 2.7 eV for $K_2TlAsCl_6$ and $K_2TlAsBr_6$, respectively, indicating a direct relationship with their optical transition energies.[19] According to our accurate observations, both halides have remarkable visible spectrum photon absorption properties, which are essential for the efficiency of opto-electronic systems.

For optical components to be successfully integrated into devices like photonic crystals, waveguides, solar cells, and

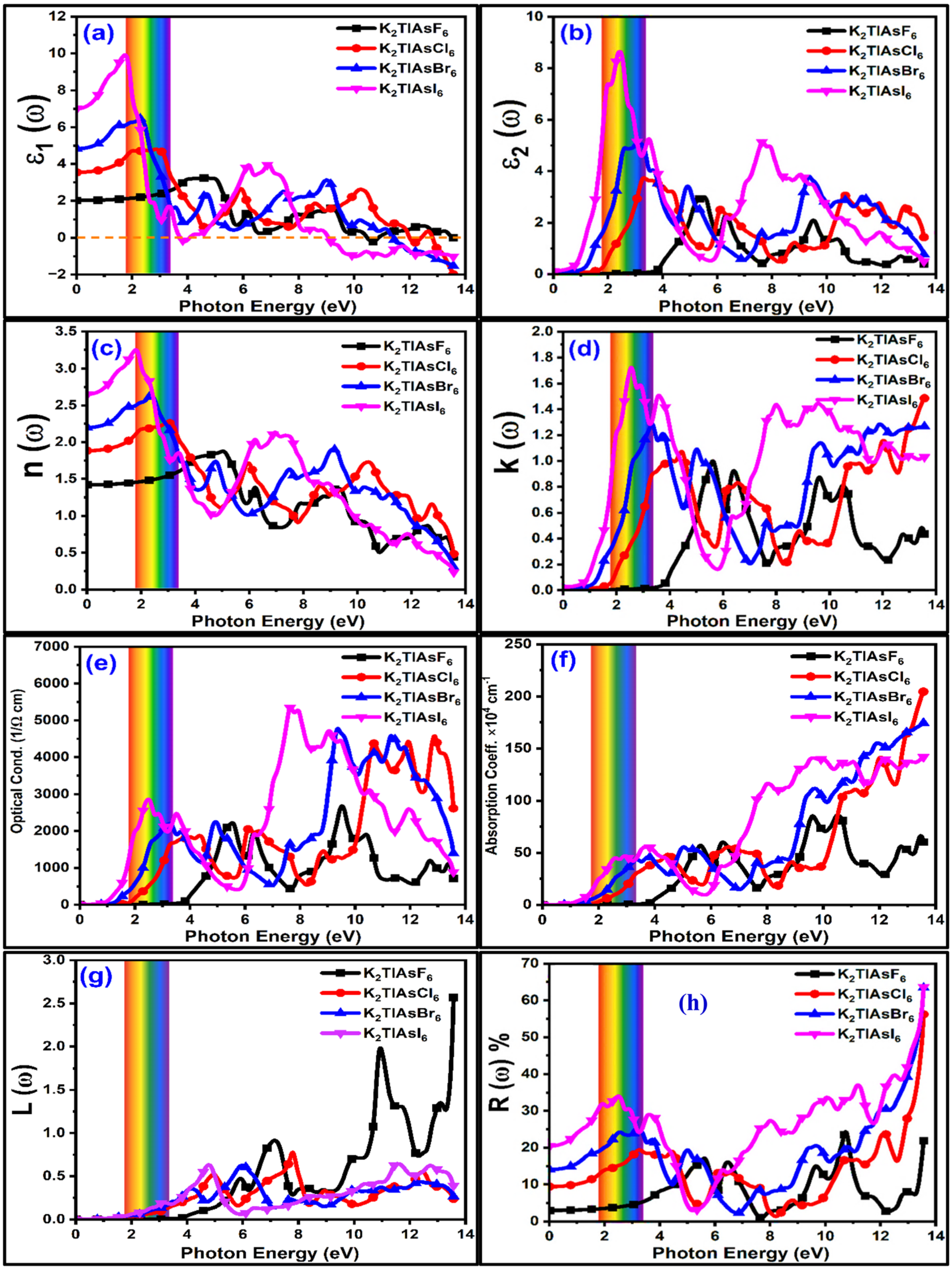

Fig. 5 (a–h) Optical properties of $K_2TlAsZ_6$ (Z = F, Cl, Br, and I) using the mBJ + SOC method.

detection devices, an extensive knowledge of the refractive index is essential. Fig. 5c depicts the variation in the refractive index for $K_2TlAsZ_6$ (Z = F, Cl, Br, and I) as a function of the photon energy. The calculated static refractive index values, *n* (0), for each composition are listed in Table 2 in comparison to the data reported by Junaid Munir *et al.* (2025).[19] As illustrated in Fig. 5c, the refractive indices of the investigated compounds exhibit an increasing trend from zero photon energy (0 eV) up to their respective maximum values of 1.87 (5.04 eV) for $K_2TlAsF_6$, 2.25 (3.08 eV) for $K_2TlAsCl_6$, 2.62 (2.32 eV) for $K_2TlAsBr_6$, and 3.24 (1.78 eV) for $K_2TlAsI_6$ as compared to the highest peak observed at 3.38 eV for $K_2TlAsCl_6$ and 2.79 eV for $K_2TlAsBr_6$, respectively.[19] Following the attainment of its peak value, the refractive index for each compound exhibits a decline across specific energy intervals. This behavior suggests a transition in the optical response of the medium from linear to nonlinear,

Table 2 Static dielectric constant for $K_2TlAsZ_6$ (Z = F, Cl, Br, and I)[a]

| Compounds | $\varepsilon_1(0)$ | $n(0)$ | $R(\omega)$ |
|---|---|---|---|
| $K_2TlAsF_6$ | 2.01 | 1.42 | 24.40% (10.73 eV) |
| $K_2TlAsCl_6$ | 3.54<br>$3.18^{A}$ | 1.88<br>$1.76^{A}$ | 24.14% (12.15 eV) |
| $K_2TlAsBr_6$ | 4.83<br>$3.75^{A}$ | 2.19<br>$2.94^{A}$ | 30.58% (12.12 eV) |
| $K_2TlAsI_6$ | 7.01 | 2.64 | 40.12% (12.47 eV) |

[a] Ref$^{A}$.[19]

thereby imparting superluminal characteristics to the material.[33] The calculated refractive index values for the double perovskites $K_2TlAsZ_6$ (Z = F, Cl, Br, and I) are found to be equal to or greater than unity, indicating that these materials exhibit linear optical behavior. As depicted in Fig. 5c (left panel), the group velocity ($V_g = c/n$) remains positive, with no indication of a transition toward negative energy. A refractive index greater than one implies a decrease in photon velocity upon entering the medium, attributed to the interaction between incident photons and the electronic structure of the material, thereby inducing a temporal delay in photon propagation. In addition, the absorption coefficient $k(\omega)$, shown in Fig. 5d, characterizes the material's capacity to attenuate incident light. The spectral profile of $k(\omega)$ follows a similar trend to that of the imaginary component of the dielectric function, $\varepsilon_2(\omega)$. The peak values of $k(\omega)$ are identified as 0.99 (5.59 eV), 1.06 (4.39 eV), 1.29 (3.33 eV), and 1.72 (2.54 eV) for $K_2TlAsZ_6$ with Z = F, Cl, Br, and I, respectively.

Electronic conduction is the cause of the optical conductivity $\sigma(\omega)$. As displayed in Fig. 5e, the first peak values of $\sigma(\omega)$ are 2679.7 $[\Omega\ \mathrm{cm}]^{-1}$ at 9.51 eV, 4578.4 $[\Omega\ \mathrm{cm}]^{-1}$ at 12.88 eV, 4768.5 $[\Omega\ \mathrm{cm}]^{-1}$ at 9.34 eV, and 5351.3 $[\Omega\ \mathrm{cm}]^{-1}$ at 7.66 eV for $K_2TlAsZ_6$ (Z = F, Cl, Br, and I), whereas the highest peak ever seen is 5351.3 $[\Omega\ \mathrm{cm}]^{-1}$ at 7.66 eV for $K_2TlAsI_6$. In the ultraviolet light spectrum, the $\sigma(\omega)$ is expected to exhibit a significant rise in the 7.6 to 13 eV region, which is essential for optoelectronic applications. Consequently, $K_2TlAsI_6$ is the best option for these applications because of its exceptional values.[37] Fig. 5f shows the absorption coefficient $\alpha(\omega)$ of $K_2TlAsZ_6$ (Z = F, Cl, Br, and I). The extent to which light may enter a material before it is fully absorbed is indicated by the symbol $\alpha(\omega)$. Each substance has a threshold at which it stops absorbing light. When photons collide with valence-state electrons, photon–electron interactions take place, which, once the threshold value is exceeded, produce very efficient light absorption. The formula shows a significant decrease in energy.[38–40]

$$\alpha = 4\pi k/\lambda \tag{7}$$

The materials $K_2TlAsZ_6$ (Z = F, Cl, Br, and I) display an upsurge in absorbance from $E_g$ (eV), reaching utmost intensities between 8 to 12 eV. The cutoff value of the absorption edge is established in the following manner: 3.60 eV for $K_2TlAsF_6$; 1.82 eV for $K_2TlAsCl_6$; 1.30 eV for $K_2TlAsBr_6$; and 0.99 eV for $K_2TlAsI_6$ as compared to the data at 2.08 eV for $K_2TlAsCl_6$ and 1.69 eV for $K_2TlAsBr_6$, respectively.[19] The apex standards for the $\alpha(\omega)$ are 85.26 cm$^{-1}$ (9.61 eV) for $K_2TlAsF_6$; 141.04 cm$^{-1}$ (12.01 eV) for $K_2TlAsCl_6$; 155.01 cm$^{-1}$ (11.90 eV) for $K_2TlAsBr_6$; and 140.59 cm$^{-1}$ (9.59 eV) for $K_2TlAsI_6$, as compared to the highest peak observed at 4.01 eV for $K_2TlAsCl_6$ and 1.87 eV for $K_2TlAsBr_6$, respectively.[19] The double perovskites under analysis show a notable rise in optical absorption in the blue (UV) shift. The in-depth examination of the spectral features confirms that $K_2TlAsZ_6$ (Z = F, Cl, Br, and I) has excellent absorption qualities, making it ideal for optoelectronic applications.

The energy emitted per unit area may be expressed as $L(\omega)$. Dispersion, thermal impacts, and plasmonic interaction are the principal factors influencing the optical loss $L(\omega)$. Fig. 5g exemplifies the reaction of the energy loss function $L(\omega)$. The most significant optical loss for $K_2TlAsZ_6$ (Z = F, Cl, Br, and I) is documented as 1.98 (10.92 eV), 0.77 (7.79 eV), 0.62 (5.97 eV), and 0.63 (4.77 eV), as compared to the highest peak observed at 7.8 eV for $K_2TlAsCl_6$ and 5.8 eV for $K_2TlAsBr_6$, respectively.[19] Fig. 5g illustrates that the $L(\omega)$ reaches its minimum as the reflectivity approaches its maximum, and *vice versa*. In the purview of visible light absorption, the $L(\omega)$ decreases. The findings demonstrate that materials $K_2TlAsZ_6$ (Z = F, Cl, Br, and I) are suitable for photonic and solar power applications.

The surface reflectivity of a solid can be assessed through $\varepsilon(\omega)$, which measures the quantity of incident sunlight that is reflected.[41] It may be represented as:

$$\text{Reflectivity}\ R(\omega) = \frac{\text{ratio of incident light}}{\text{ratio of reflected light}} = \left|\frac{(\varepsilon_1(\omega) + \mathrm{i}\varepsilon_2(\omega))^{1/2} - 1}{(\varepsilon_1(\omega) + \mathrm{i}\varepsilon_2(\omega))^{1/2} + 1}\right|^2 \tag{8}$$

Fig. 5h illustrates the depicted reflectivities $R(\omega)$ of DP $K_2TlAsZ_6$ (Z = F, Cl, Br, and I). The $R(\omega)$ of the DPs vary at diverse light energies (in eV): 24.10% (10.70 eV) for $K_2TlAsF_6$, 23.19% (12.23 eV) for $K_2TlAsCl_6$, 30.61% (12.09 eV) for $K_2TlAsBr_6$, and 39.65% (12.47 eV) for $K_2TlAsI_6$, respectively.

### 3.5 Thermoelectric properties

**3.5.1 Thermoelectric properties *vs.* temperature.** Thermopower can elucidate a material's thermoelectric characteristics. When a change in the internal temperature of a substance induces an electromotive force, the phenomenon occurs. Electrical conductivity EC ($\sigma$), power factor (PF), Seebeck coefficient ($S$), figure of merit ($ZT$), and electronic thermal conductivity ($\kappa_e$) serve as principal metrics for elucidating thermoelectric properties through band structure analysis. Consequently, the values for $K_2TlAsZ_6$ (Z = F, Cl, Br, and I) were determined over the $T$ (K) of 100–1000 K, as illustrated in Fig. 6a–e.

The generated electric potential in a compound when exposed to a temperature differential is predicted by the Seebeck coefficient ($S$), a thermoelectric characteristic. Fig. 6(a) for $K_2TlAsZ_6$ (Z = F, Cl, Br, and I) DPs displays the computed $S$ *versus* temperature. All of the temperature ranges under consideration have positive values for $S$. Consequently, like the majority of DPs, $K_2TlAsZ_6$ (Z = F, Cl, Br, and I) DPs are p-type

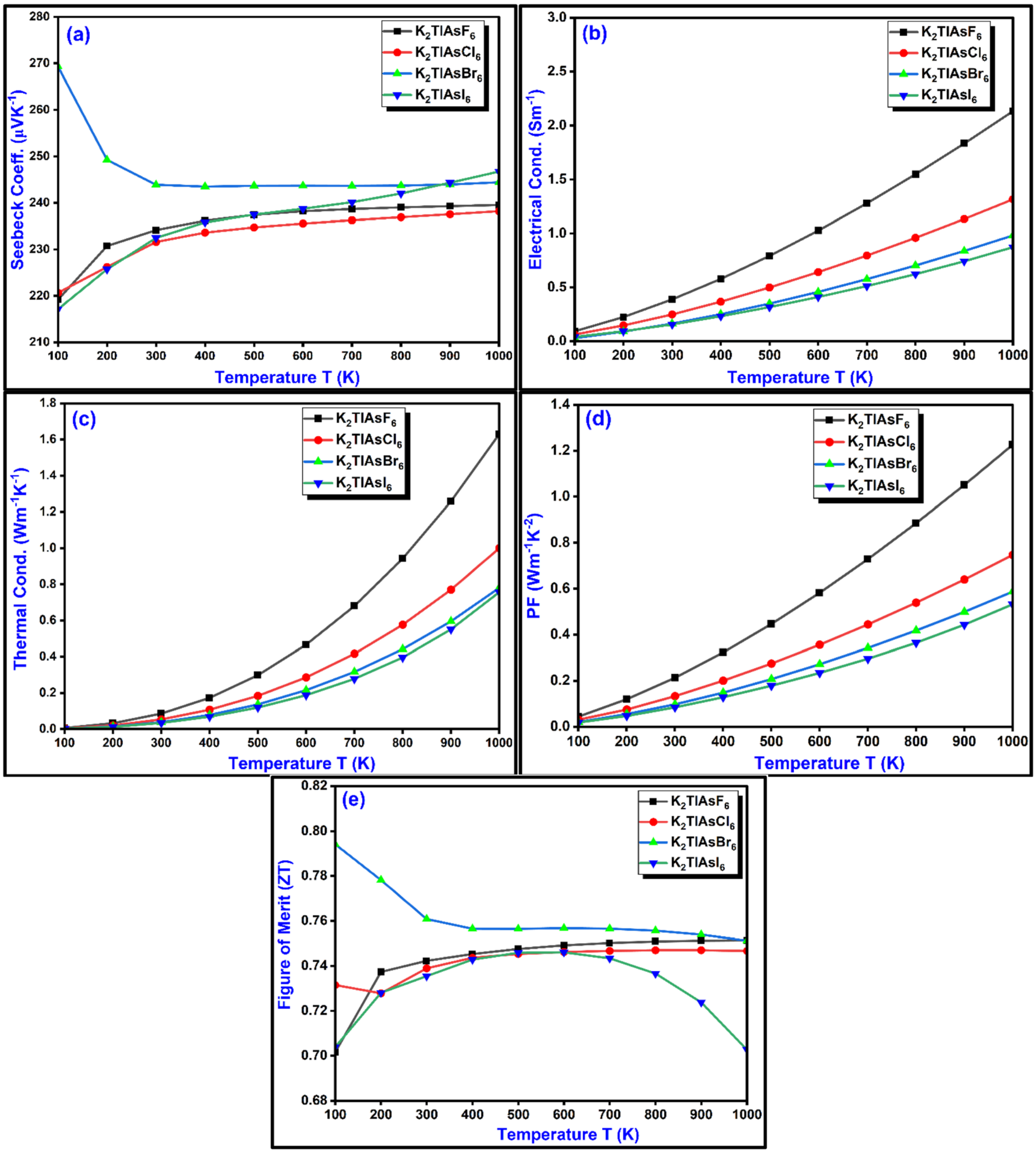

Fig. 6 (a–e) Thermoelectric properties *vs.* temperature of $K_2TlAsZ_6$ (Z = F, Cl, Br, and I) using the TB-mBJ method.

Table 3 Thermoelectric data of the $K_2TlAsZ_6$ (Z = F, Cl, Br, and I) DPs[a]

| Compounds | $K_2TlAsF_6$ | | $K_2TlAsCl_6$ | | $K_2TlAsBr_6$ | | $K_2TlAsI_6$ | |
|---|---|---|---|---|---|---|---|---|
| Temperature | 300 K | 1000 K | 300 K | 1000 K | 300 K | 1000 K | 300 K | 1000 K |
| $S$ (μV K$^{-1}$) | 234.17 | 239.54 | 231.63<br>$238^{A}$ | 238.21 | 243.89<br>$254^{A}$ | 244.42 | 232.50 | 246.74 |
| $\sigma$ (S m$^{-1}$) | 38.77 | 213.50 | 24.77 | 131.59 | 16.28 | 98.17 | 15.52 | 87.30 |
| $\kappa_e$ (Wm$^{-1}$ K$^{-1}$) | 85.93 | 1630.35 | 53.96 | 1000.00 | 38.19 | 780.64 | 34.22 | 756.44 |
| PF | 0.21 | 1.23 | 0.13 | 0.75 | 0.10 | 0.59 | 0.08 | 053 |
| $ZT$ | 0.74 | 0.75 | 0.73<br>$0.75^{A}$ | 0.74 | 0.76<br>$0.99^{A}$ | 0.75 | 0.73 | 0.70 |

[a] Ref$^{A}$.[19]

semiconductors.[42–44] Moreover, the $S$-value for DPs falls as the temperature escalates. Table 3 displays, accordingly, the calculated values of $S$ for $K_2TlAsZ_6$ (Z = F, Cl, Br, and I). Fig. 6(a) shows that at 300 K, $S$ values for $K_2TlAsZ_6$ (Z = F, Cl, Br, and I); at higher temperatures, the $S$ values for the $K_2TlAsZ_6$ (Z = F, Cl, Br, and I) compounds decline. There have also been reports of this kind of fluctuation in $S$ for other DPs, when $F$ is replaced at the X-site by Cl, Br or I, respectively.[45]

A crucial thermoelectric characteristic, $\sigma/\tau$, measures the amount of charge carriers that may be transported through a material. Fig. 6(b) displays the computed $\sigma/\tau$ that is dependent on temperature for the $K_2TlAsZ_6$ (Z = F, Cl, Br, and I) compounds. DPs follow the same trend as the other semiconductors, in that $\sigma/\tau$ grows linearly with temperature. This is because a greater number of charge carriers become accessible for conductivity as temperatures rise. Table 3 presents the $\sigma/\tau$ values calculated for $K_2TlAsZ_6$ (Z = F, Cl, Br, and I). The greater band gap is the main reason why $K_2TlAsF_6$ has greater $\sigma$ values compared to other compounds. The relationship between the $\sigma$ and the carrier concentration ($N$) may be expressed as $\sigma = Ne\mu$.

The temperature-dependent $\kappa_e$ is shown in Fig. 6(c) as having greater values for the $K_2TlAsF_6$ compound compared to other compounds. One possible explanation is that $K_2TlAsF_6$ has a greater band gap than other compounds. The band gap has also been shown to cause this kind of $\kappa_e$ change in other DPs.[45,46] On the other hand, similar to other types of semiconductors, the values of $\kappa_e$ DPs grow as the temperature rises.[13,47] The highest $\kappa_e$ values for $K_2TlAsZ_6$ (Z = F, Cl, Br, and I) at the temperatures of 300 K and 1000 K are summarized in Table 3.

The power factor (PF) precisely computes the thermoelectric functionality of a material, which is expressed by:

$$\mathrm{PF} = S^2 \times \sigma \tag{9}$$

The relationship among the Seebeck coefficients ($S$) and electrical conductivity ($\sigma$) is described in eqn (9). Fig. 6d shows the PF *vs.* $T$ (K) data for the $K_2TlAsZ_6$ (Z = F, Cl, Br, and I) compounds, depicting the potential use of these compounds in thermoelectric devices with a PF of one or greater than unity.[48,49] The PF values increase linearly with the upturn in temperature from 300 K to 1000 K. The decrease in the ($S$) and surge in the EC ($\sigma$) may be due to the variation in the temperature, affecting the PF metrics for the $K_2TlAsZ_6$ (Z = F, Cl, Br, and I) DPs. The PF values at different temperatures are given in Table 3.

A material's figure of merit ($ZT$) is a compilation of its thermoelectric efficiency, which is determined as follows:[50]

$$ZT = \frac{S^2\sigma T}{\kappa_e + \kappa_L} \tag{10}$$

For the $ZT$ values to be high, the denominator ($\kappa_e$) must be low, while $S$ and $\sigma$ must be high. Fig. 6(e) displays the computed $ZT$ for $K_2TlAsZ_6$ (Z = F, Cl, Br, and I). When the temperature is elevated to 1000 K, the $ZT$ standards for $K_2TlAsZ_6$ (Z = F, Cl, Br, and I) reach 0.75, 0.74, 0.75, and 0.70, respectively. A prominent aspect of DPs is this rising tendency in $ZT$ with temperature.[51] Although some predictable DPs have lower $ZT$ standards, $K_2TlAsZ_6$ (Z = F, Cl, Br, and I) DPs have maximum $ZT$ standards.[52] Thus, $K_2TlAsZ_6$ (Z = F, Cl, Br, and I) are promising materials for thermoelectric power generation.

**3.5.2 Thermoelectric properties *vs.* chemical potential.** The transport properties of $K_2TlAsZ_6$ (Z = F, Cl, Br, and I) compounds were systematically investigated over a broad temperature range to assess their thermoelectric performance. The chemical potential ($\mu - E_F$) was analyzed at fixed temperatures of 300 K, 500 K, 700 K, and 1000 K. In this context, the transport behavior associated with the heavy valence bands was evaluated within the framework of Boltzmann transport theory. The Boltz-Trap[53] computational tools were employed to determine the Seebeck coefficient, as well as the electrical and thermal conductivities, aiming to evaluate the power conversion efficiency of the $K_2TlAsZ_6$ (Z = F, Cl, Br, and I) compounds. The Seebeck coefficient of the $K_2TlAsZ_6$ (Z = F, Cl, Br, and I) compounds was calculated as a function of the chemical potential at fixed temperatures of 300 K, 500 K, 700 K, and 1000 K, as presented in Fig. 7a–d. A systematic decrease in the Seebeck coefficient is observed with increasing temperature.[54] The Seebeck coefficient is found to be notably higher for p-type carriers across the investigated compounds. For the series $K_2TlAsZ_6$ (Z = F, Cl, Br, and I), the maximum values of the Seebeck coefficient generally appear away from the Fermi level, except in the case of $K_2TlAsF_6$, where the peak is observed in closer proximity to the Fermi level. At 300 K, the highest Seebeck coefficients for the $K_2TlAsZ_6$ compounds are calculated as 265.20 $\mu V K^{-1}$, 254.63 $\mu V K^{-1}$, 182.39 $\mu V K^{-1}$, and 126.03 $\mu V K^{-1}$, for Z = F, Cl, Br, and I, respectively.[55]

Semiconducting compounds exhibit pronounced sensitivity to temperature gradients; whereby elevated temperatures promote the excitation of charge carriers from the valence band (VB) to the conduction band (CB). This thermal activation results in an increased carrier concentration across the VB and CB gap. The dependence of electrical conductivity ($\sigma$) on the chemical potential ($\mu - E_F$) is presented in Fig. 7a–d.

As illustrated in Fig. 7a–d, the $\sigma/\tau$ ratio exhibits an increasing trend with temperature at lower chemical potentials. Conversely, at higher chemical potentials, $\sigma/\tau$ decreases as the temperature rises. This behavior is in agreement with the theoretical expectations for intrinsic semiconductors. For the investigated $K_2TlAsZ_6$ (Z = F, Cl, Br, and I) double perovskite compounds, the calculated results reveal that the electrical conductivity is more significantly enhanced under negative ($\mu - E_F$) conditions than under positive ($\mu - E_F$) shifts relative to the Fermi level.[56]

The dependence of $\kappa_e/\tau$ on the chemical potential exhibits a trend analogous to that of $\sigma/\tau$, albeit with a more pronounced temperature dependence. This discrepancy can be attributed to the Wiedemann–Franz law ($\kappa_e = L_\sigma T$), which relates the electronic thermal conductivity to the electrical conductivity by means of the Lorentz number ($L$).[57] This trend further reveals that the $\kappa_e$ to $\tau$ ratio increases with temperature, as clearly depicted in Fig. 7a–d, thereby validating the reliability of the computed results.

To assess the performance of the compounds under study, the power factor (PF) was calculated using the relation (PF =

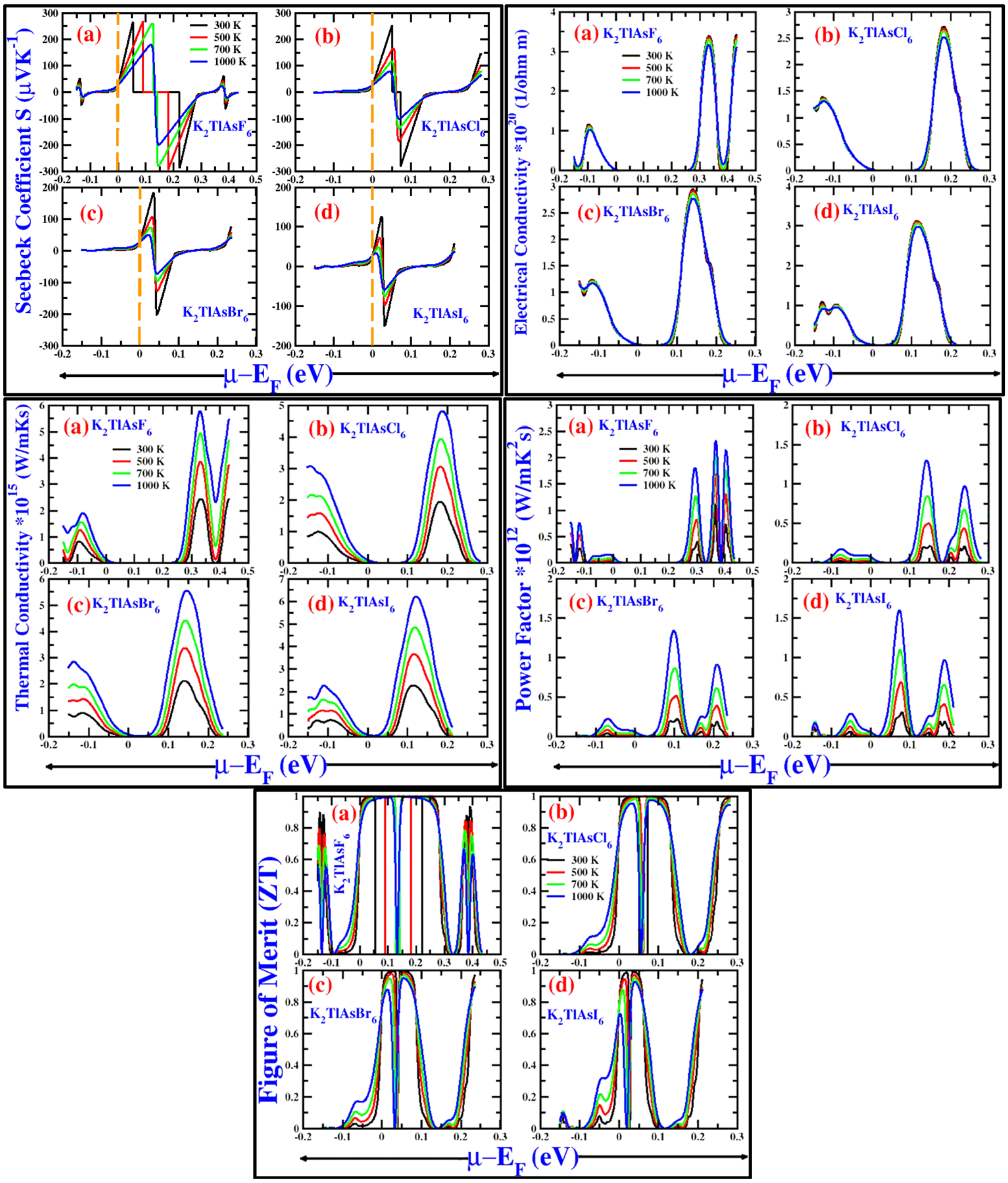

Fig. 7 Thermoelectric properties *vs.* chemical potential of $K_2TlAsZ_6$ (Z = F, Cl, Br, and I) using the TB-mBJ method.

Table 4 Gibbs free energy $G^*$ ($\times 10^7$) [kJ mol$^{-1}$] and Entropy ($S$) [J mol$^{-1}$ K$^{-1}$] of $K_2TlAsZ_6$ (Z = F, Cl, Br, and I)

| | | Gibbs free energy $G^*$ ($\times 10^7$) [kJ mol$^{-1}$] | | | | Entropy ($S$) [J mol$^{-1}$ K$^{-1}$] | | | |
|---|---|---|---|---|---|---|---|---|---|
| Compounds | Pressure | 300 K | 500 K | 700 K | 1000 K | 300 K | 500 K | 700 K | 1000 K |
| $K_2TlAsF_6$ | 0 GPa | −6.394 | −6.394 | −6.394 | −6.394 | 346.946 | 482.670 | 578.845 | 689.461 |
| | 10 GPa | −6.393 | −6.394 | −6.394 | −6.394 | 259.326 | 385.177 | 473.546 | 571.786 |
| $K_2TlAsCl_6$ | 0 GPa | −6.960 | −6.960 | −6.960 | −6.960 | 410.583 | 548.675 | 646.129 | 758.499 |
| | 10 GPa | −6.960 | −6.960 | −6.960 | −6.960 | 287.857 | 414.489 | 502.298 | 599.054 |
| $K_2TlAsBr_6$ | 0 GPa | −1.034 | −1.034 | −1.034 | −1.034 | 468.737 | 607.868 | 705.701 | 818.426 |
| | 10 GPa | −1.034 | −1.034 | −1.034 | −1.034 | 333.206 | 461.502 | 549.534 | 646.041 |
| $K_2TlAsI_6$ | 0 GPa | −1.744 | −1.744 | −1.744 | −1.744 | 522.761 | 662.775 | 761.152 | 874.695 |
| | 10 GPa | −1.744 | −1.744 | −1.744 | −1.744 | 368.341 | 497.301 | 585.192 | 681.141 |

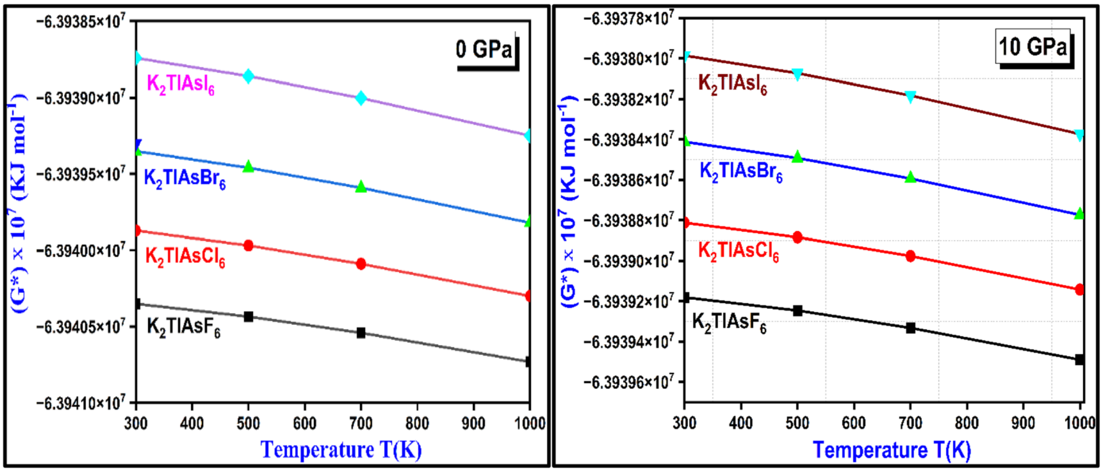

Fig. 8 (a and b) Gibbs free energy ($G^*$) (kJ mol$^{-1}$) of $K_2TlAsZ_6$ (Z = F, Cl, Br, and I).

$S^2\sigma$), where $S$ is the Seebeck coefficient and $\sigma$ is the electrical conductivity. This parameter reflects the efficiency of a material in converting thermal energy into electrical power. Fig. 7a–d illustrates the variation of the chemical potential with respect to PF for the $K_2TlAsZ_6$ (Z = F, Cl, Br, and I) compounds. The results indicate that with increasing temperature from 300 K to 1000 K, the peak positions of PF shift away from the Fermi level and exhibit an increase in magnitude. This trend suggests that elevated temperatures and moderate carrier concentrations contribute to an enhancement in the power factor. Additionally, it is observed that the maximum PF values are located in the p-type region, indicating that these compounds possess significant potential for application as p-type thermoelectric materials. The relationship between $ZT$ and chemical potential is also depicted in Fig. 7a–d. Fig. 7a–d depicts the decrease in the thermoelectric efficiency (Figure of Merit) $ZT$ value for $K_2TlAsZ_6$ (Z = F, Cl, Br, and I), respectively. The peak nearly reaches unity. The gradual decrease in the $ZT$ metrics with increasing temperature indicates the peaks approaching unity (1.0) within the lower temperature limits (300 K).[55,58]

## 3.6 Thermodynamic calculations

**3.6.1 Gibbs free energy ($G^*$).** The Gibbs free energy ($G^*$) is specified by the relation $G^* = H - TS$, where H denotes the enthalpy, $T$ is the absolute temperature, and $S$ represents the entropy, and is a crucial parameter for assessing the stability of materials under varying temperature and pressure (see Table 4). For the $K_2TlAsZ_6$ (Z = F, Cl, Br, and I) series, analyzing the Gibbs free energy ($G^*$) as a function of these variables provides critical insights into their thermal and mechanical stability. Fig. 8(a and b demonstrates that at both pressure levels, the Gibbs free energy ($G^*$) falls as the temperature rises from 200–600 K. Since the entropy component ($-TS$) decreases the free energy as the temperature increases, this pattern is consistent with theory. At all temperatures, the Gibbs free energy values are somewhat less negative at 10 GPa than they are at 0 GPa, indicating

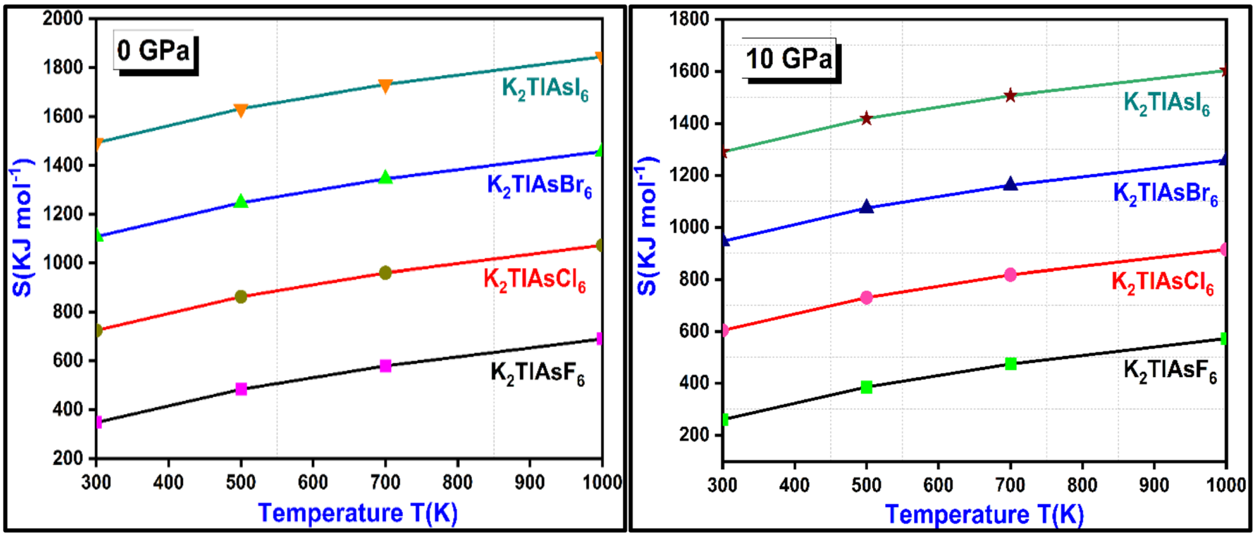

Fig. 9 (a and b) Entropy $S$ (J mol$^{-1}$ K$^{-1}$) of $K_2TlAsZ_6$ (Z = F, Cl, Br, and I).

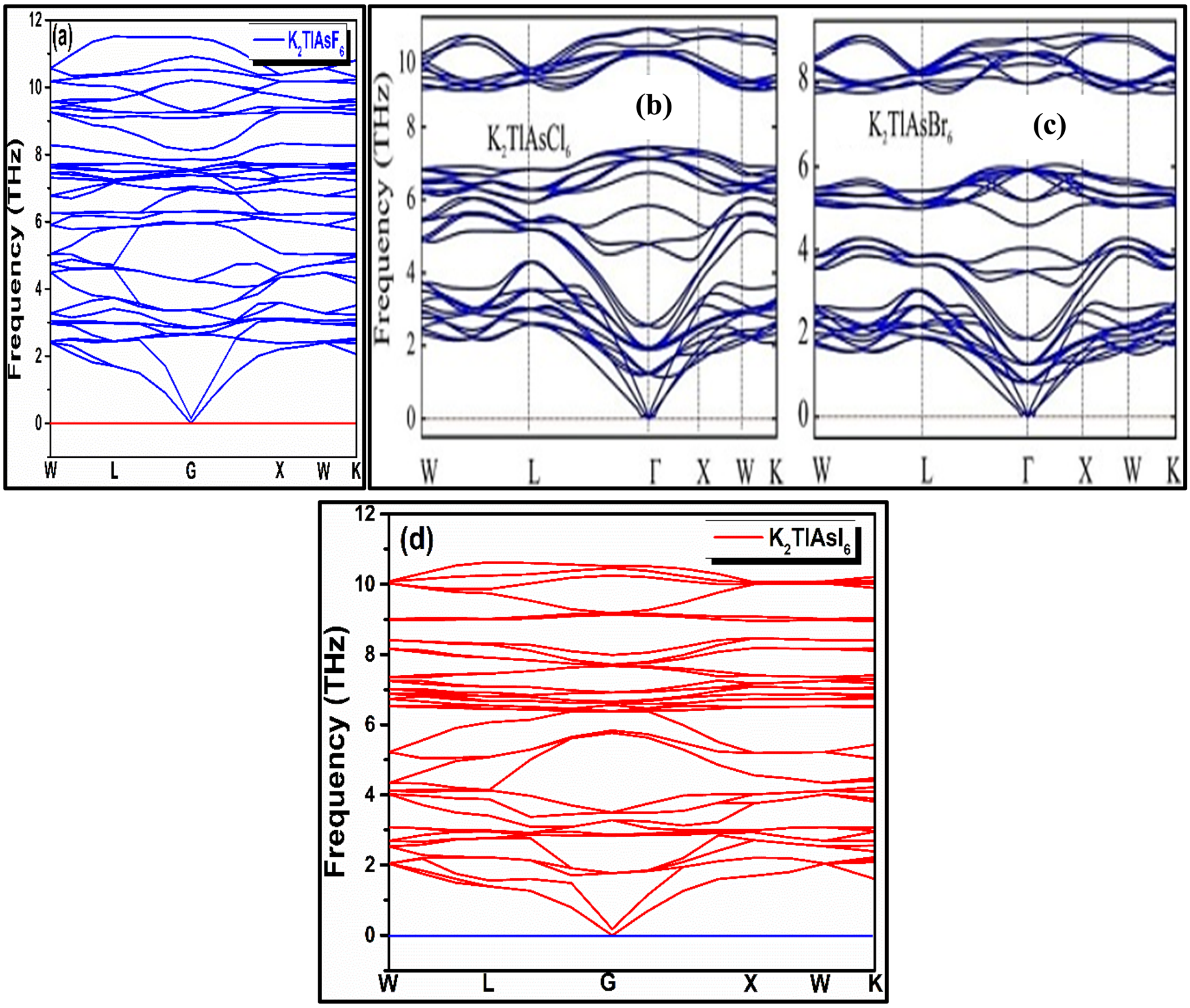

Fig. 10 (a–d) Phonon curves of $K_2TlAsZ_6$ (Z = F, Cl, Br, and I).

a minor reduction in thermodynamic stability under higher pressure (see Table 4). Nevertheless, the small differences between the two pressure conditions suggest that the $K_2TlAsZ_6$ (Z = F, Cl, Br, and I) compounds maintain thermodynamic stability over the entire range of temperatures and pressures examined.[59,60]

**3.6.2 Entropy.** Fig. 9a and b depicts the temperature dependence of entropy for $K_2TlAsZ_6$ (Z = F, Cl, Br, and I) under pressures of 0 GPa and 10 GPa, highlighting the essential thermodynamic characteristics (see Table 4). For all compositions and pressures, entropy increases consistently with temperature. This behavior is attributed to enhanced kinetic energy at elevated temperatures, which allows access to a greater number of microstates, thereby increasing the system's disorder. Conversely, entropy exhibits a clear negative correlation with pressure. At a fixed temperature, increasing the pressure from 0 GPa to 10 GPa results in a reduction of entropy (see Table 4). This effect arises from the material's compression under pressure, which constrains atomic and molecular movement, reduces the available phase space for configurations, and thus lowers the overall disorder.[61]

The equation for the entropy using the Debye–Slater model is expressed as:

$$S = -3nk_B \quad \ln(1 - e^{-\theta_D/T}) + 4nk_B D(\theta_D/T) \tag{11}$$

### 3.7 Phonon dispersion

By utilizing the density functional perturbation theory (DFPT), the phonon dispersion band structures associated with high symmetry points in the 1st Brillouin zone for $K_2TlAsF_6$, $K_2TlAsCl_6$, $K_2TlAsBr_6$, and $K_2TlAsI_6$ are computed and displayed in Fig. 10. For this purpose, Phonopy code is used, which is employed through Wien2K.[61] Due to the presence of 10 atoms per unit cell, there are three acoustic modes, *i.e.*, one longitudinal and two transverse, and 27 optical modes, which are classified as low frequency and high frequency phonons, respectively. Positive phonon frequencies, as depicted from the curves, have been used to confirm the thermodynamic stability of $K_2TlAsF_6$, $K_2TlAsCl_6$, $K_2TlAsBr_6$, and $K_2TlAsI_6$ at higher frequencies, reaching 11 and 9 THz. The phonon gap is visible in optical modes for all double perovskites.[19]

# 4 Conclusion

Using density functional theory (DFT) computations, this work examines the optoelectronic and photovoltaic characteristics of $K_2TlAsZ_6$ (Z = F, Cl, Br, and I). Calculated tolerance factors and formation energies were used to assess the structural stability of both compounds; these values together show their dynamic stability. The generalized gradient approximation (GGA) using the PBE for solids (GGA-PBEsol) functional were used to optimize physical parameters. The Trans and Blaha modified Becke–Johnson (mBJ) and spin orbit coupling (SOC) potentials were then used to compute precise band gap values. Both substances have $K_2TlAsZ_6$ (Z = F, Cl, Br, and I) values between 3.25 eV and 0.37 eV, indicating that they are direct band gap semiconductors. These values have significant potential for use in optoelectronic devices since they fall between the infrared to ultraviolet area of the electromagnetic spectrum. The thermodynamic study demonstrates that entropy and the Gibbs free energy decrease with increasing pressure and increase with rising temperature. The $K_2TlAsZ_6$ (Z = F, Cl, Br, and I) compounds are interesting prospects for upcoming optical and photovoltaic applications because of their straight band-gap, enhanced optical conductivity, and prominent absorption coefficients in the UV-region of the EM spectrum. The high *ZT* for the compounds $K_2TlAsBr_6$ and $K_2TlAsI_6$, except $K_2TlAsZ_6$ (Z = F and Cl), indicates the use of these materials as thermoelectric devices.

# Conflicts of interest

There are no conflicts to declare.

# Data availability

Data can be made available on reasonable request.

Supplementary information is available. See DOI: **https://doi.org/10.1039/d5ra05932a**.

# References

1 Q. Mahmood, T. Ghrib, A. Rached, A. Laref and M. Kamran, Probing of mechanical, optical and thermoelectric characteristics of double perovskites Cs2GeCl/Br6 by DFT method, *Mater. Sci. Semicond. Process.*, 2020, **112**, 105009.
2 S. Kumari, *et al.*, Progress in theoretical study of lead-free halide double perovskite $Na_2AgSbX_6$ (X = F, Cl, Br, and I) thermoelectric materials, *J. Mol. Model.*, 2023, **29**(6), 195.
3 M. U. Din, J. Munir, T. Alshahrani, H. Elsaeedy and Q. Ain, Scrutinized the spin-orbit coupling effect on the elastically and thermodynamically stable Rb2BCl6 (B= Pb, Ti) double perovskites for photocatalytic, optoelectronic and renewable energy applications, *Mater. Sci. Semicond. Process.*, 2023, **163**, 107569.
4 S. M. Qaid, H. M. Ghaithan, H. S. Bawazir and A. S. Aldwayyan, Simple approach for crystallizing growth of $MAPbI_3$ perovskite nanorod without thermal annealing for Next-Generation optoelectronic applications, *Mater. Chem. Phys.*, 2023, **298**, 127423.
5 J. Munir, *et al.*, Electronic structure and optical and thermoelectric response of lead-free double perovskite $BaMgLaBiO_6$: a first-principles study, *J. Comput. Electron.*, 2023, **22**(5), 1482–1494.
6 S.-H. Turren-Cruz, A. Hagfeldt and M. Saliba, Methylammonium-free, high-performance, and stable perovskite solar cells on a planar architecture, *Science*, 2018, **362**(6413), 449–453.
7 S. A. Dar, V. Srivastava, U. K. Sakalle, A. Rashid and G. Pagare, First-principles investigation on electronic structure, magnetic, mechanical and thermodynamic properties of $SrPuO_3$ perovskite oxide, *Mater. Res. Express*, 2018, **5**(2), 026106.
8 S. M. Qaid and A. S. Aldwayyan, Aprotic solvent effect in preparation of organo lead iodide perovskite nanowires by two-step spin-coating procedure, *ECS J. Solid State Sci. Technol.*, 2023, **12**(2), 026004.
9 H. S. Bawazir, S. M. Qaid, H. M. Ghaithan, K. K. AlHarbi, A. F. Bin Ajaj and A. S. Aldwayyan, Phase state influence on photoluminescence of MAPb $(Br_xI_{1-x})_3$ perovskites towards optimized photonics applications, *Photonics*, 2022, **10**(1), 21.
10 G. Pilania, P. V. Balachandran, C. Kim and T. Lookman, Finding new perovskite halides via machine learning, *Front. Mater.*, 2016, **3**, 19.
11 P. Han, *et al.*, Lead-free sodium–indium double perovskite nanocrystals through doping silver cations for bright yellow emission, *Angew. Chem.*, 2019, **131**(48), 17391–17395.
12 P. A. Nawaz, *et al.*, Theoretical investigations of optoelectronic and transport properties of $Rb_2YInX_6$ (X= Cl, Br, I) double perovskite materials for solar cell applications, *Sol. Energy*, 2022, **231**, 586–592.
13 M. W. Iqbal, *et al.*, Tuning of the electronic bandgap of lead-free double perovskites $K_2AgBiX_6$ (X = Cl, Br) for solar cells applications and their thermoelectric characteristics, *Sol. Energy*, 2022, **239**, 234–241.
14 N. A. Kattan, *et al.*, Tuning of band gap by anion variation of double perovskites $K_2AgInX_6$ (X = Cl, Br) for solar cells and thermoelectric applications, *J. Solid State Chem.*, 2023, **319**, 123820.
15 N. Erum, J. Ahmad, M. A. Iqbal and M. Ramzan, DFT insights of mechanical, optoelectronic and thermoelectric properties for $Cs_2ScTlX_6$ (X = Cl, Br, I) double perovskites, *Opt. Quantum Electron.*, 2023, **55**(4), 337.
16 W. Zhou, T. Cui, Z. Zhang, Y. Yang, H. Yi and D. Hou, Measurement of wide energy range neutrons with a CLYC (Ce) scintillator, *J. Instrum.*, 2023, **18**(02), P02014.
17 G. Murtaza, *et al.*, Tailoring of band gap to tune the optical and thermoelectric properties of Sr1-xBaxSn$O_3$ stannates for clean energy; probed by DFT, *Chem. Phys.*, 2021, **551**, 111322.

18 Q. Mahmood, *et al.*, Study of lead-free double perovskites $X_2AgBiI_6$ (X = K, Rb, Cs) for solar cells and thermoelectric applications, *J. Mater. Res. Technol.*, 2023, **22**, 913–922.

19 J. Munir, I. Mursaleen, H. M. Ghaithan, Q. ul Ain, A. A. A. Ahmed and S. M. Qaid, First-principles investigations of the mechanically and thermodynamically stable potassium-based double perovskites $K_2TlAsX_6$ (X = Cl, Br) for optoelectronic and renewable applications, *Mater. Sci. Eng., B*, 2023, **298**, 116830.

20 P. Blaha, K. Schwarz, G. K. Madsen, D. Kvasnicka and J. Luitz, , WIEN2k: an APW+ lo program for calculating the properties of solidsJ. Chem. Phys., 2020, **152**, 1.

21 Z. Wu and R. E. Cohen, More accurate generalized gradient approximation for solids, *Phys. Rev. B: Condens. Matter Mater. Phys.*, 2006, **73**(23), 235116.

22 J. P. Perdew, K. Burke and M. Ernzerhof, Generalized gradient approximation made simple, *Phys. Rev. Lett.*, 1996, **77**(18), 3865.

23 P. E. Blöchl, O. Jepsen and O. K. Andersen, Improved tetrahedron method for Brillouin-zone integrations, *Phys. Rev. B: Condens. Matter Mater. Phys.*, 1994, **49**(23), 16223.

24 Y. Saeed, *et al.*, $Cs_2NaGaBr_6$: a new lead-free and direct band gap halide double perovskite, *RSC Adv.*, 2020, **10**(30), 17444–17451.

25 A. E. Fedorovskiy, N. A. Drigo and M. K. Nazeeruddin, The role of Goldschmidt's tolerance factor in the formation of $A_2BX_6$ double halide perovskites and its optimal range, *Small Methods*, 2020, **4**(5), 1900426.

26 M. Saeed, *et al.*, Optical and transport properties of novel $X_2BAgCl_6$ (where X = K, Rb, Cs, and B = Sc, Y) double perovskites, *Mater. Sci. Eng., B*, 2024, **308**, 117556.

27 N. Israr, W. u. Rehman, M. A. Jehangir, N. A. EL-Gawaad and U. Farooq, First-Principles Investigation of Narrow Bandgap Halide Double Perovskites $A_2AgSbI_6$ (A = K, Rb), *J. Inorg. Organomet. Polym. Mater.*, 2025, 1–16.

28 N. Noor, *et al.*, Analysis of direct band gap $A_2ScInI_6$ (A= Rb, Cs) double perovskite halides using DFT approach for renewable energy devices, *J. Mater. Res. Technol.*, 2021, **13**, 2491–2500.

29 Y. Saeed, *et al.*, Correction: $Cs_2NaGaBr_6$: a new lead-free and direct band gap halide double perovskite, *RSC Adv.*, 2020, **10**(34), 20196.

30 H. Fatihi, *et al.*, Enhancing Solar cell efficiency: a comparative study of lead-free double halide perovskites $Rb_2CuAsBr_6$ and $Rb_2TlAsBr_6$ using DFT and SLME methods, *J. Inorg. Organomet. Polym. Mater.*, 2025, **35**(2), 964–977.

31 B. Alsobhi, DFT insights on the chloride double perovskites $X_2AuBiCl_6$ (X = K, Rb, and Cs) with semiconductor nature for PV and optoelectronic applications, *Comput. Condens. Matter*, 2025, **43**, e01040.

32 S. Hayat, *et al.*, Investigating optical, electronic, and thermoelectric properties of $X_2ScIO_6$ (X = K, Rb, and Cs) double perovskite semiconductors for green energy applications, *Comput. Theor. Chem.*, 2025, **1243**, 114992.

33 M. A. Ali, A. A. Alothman, M. Mushab, A. Khan and M. Faizan, DFT insight into structural, electronic, optical and thermoelectric properties of eco-friendly double perovskites $Rb_2GeSnX_6$ (X = Cl, Br) for green energy generation, *J. Inorg. Organomet. Polym. Mater.*, 2023, **33**(11), 3402–3412.

34 H. Ehrenreich and H. Philipp, Optical properties of Ag and Cu, *Phys. Rev.*, 1962, **128**(4), 1622.

35 D. R. Penn, Wave-number-dependent dielectric function of semiconductors, *Phys. Rev.*, 1962, **128**(5), 2093.

36 A. N. Khan, *et al.*, Evaluating $A_2SrGeI_6$ (A = K and Rb) Lead-Free double Perovskites: Structural, Elastic, and optoelectronic insights for clean energy, *Inorg. Chem. Commun.*, 2025, **174**, 113949.

37 S. H. Shah, *et al.*, DFT investigation on thermoelectric, electronic, optoelectronic, elastic, and structural properties of sodium-based halide double perovskites $Rb_2NaSbZ_6$ (Z = Cl, Br, and I), *J. Chin. Chem. Soc.*, 2025, **72**(2), 211–228.

38 M. Hassan, A. Shahid and Q. Mahmood, Structural, electronic, optical and thermoelectric investigations of antiperovskites $A_3SnO$ (A = Ca, Sr, Ba) using density functional theory, *Solid State Commun.*, 2018, **270**, 92–98.

39 Q. Mahmood, M. Hassan, K. Bhamu, M. Yaseen, S. Ramay and A. Mahmood, Density functional theory-based study of the magnetic and optical properties of $PbMO_3$ (M= Cr, Fe) using the modified BeckeJohnson mBJ functional, *J. Phys. Chem. Solids*, 2019, **128**, 275–282.

40 M. Rashid, F. Aziz, Q. Mahmood, N. A. Kattan and A. Laref, Pressure-induced modifications in the optoelectronic and thermoelectric properties of $MgHfO_3$ for renewable energy applications, *Arabian J. Sci. Eng.*, 2022, **47**(1), 777–785.

41 A. A. Khan, A. U. Rehman, A. Laref, M. Yousaf and G. Murtaza, Structural, optoelectronic and thermoelectric properties of ternary $CaBe_2X_2$ (X = N, P, As, Sb, Bi) compounds, *Z. Naturforsch. A*, 2018, **73**(10), 965–973.

42 H. Bendjilali, A. Chahed, H. Rozale, M. Bousahla and Y. Khachai, Structural, Electronic, Elastic, Mechanical, Optical and Thermoelectric Properties of the Chalcogenide Double Perovskites A2GaNbS6 (A = Ca, Sr and Ba): Insights From Density Functional Theory Calculations, *Annals of the West University of Timisoara. Physics Series*, 2022, **64**(1), 37–54.

43 S. Bouhmaidi, A. Harbi, R. K. Pingak, A. Azouaoui, M. Moutaabbid and L. Setti, First-principles calculations to investigate lead-free double perovskites $CsInSbAgX_6$ (X = Cl, Br and I) for optoelectronic and thermoelectric applications, *Comput. Theor. Chem.*, 2023, **1227**, 114251.

44 S. Berri, Thermoelectric properties of $A_2BCl_6$: a first principles study, *J. Phys. Chem. Solids*, 2022, **170**, 110940.

45 M. A. Amin, *et al.*, Study of double perovskites $X_2InSbO_6$ (X = Sr, Ba) for renewable energy; alternative of organic-inorganic perovskites, *J. Mater. Res. Technol.*, 2022, **18**, 4403–4412.

46 F. Aslam, H. Ullah and M. Hassan, Theoretical investigation of $Cs_2InBiX_6$ (X = Cl, Br, I) double perovskite halides using first-principle calculations, *Mater. Sci. Eng., B*, 2021, **274**, 115456.

47 A. Aziz, *et al.*, Physical properties of $Sr_2MWO_6$ (M= Ca, Mg) for renewable energy applications, *Phys. Status Solidi B*, 2022, **259**(10), 2200074.

48 H. R. Aliabad, M. Ghazanfari, I. Ahmad and M. Saeed, Ab initio calculations of structural, optical and thermoelectric properties for CoSb3 and $ACo_4Sb_{12}$ (A= La, Tl and Y) compounds, *Comput. Mater. Sci.*, 2012, **65**, 509–519.

49 S. Niaz, M. A. Khan, N. Noor, H. Ullah and R. Neffati, Bandgap tuning and thermoelectric characteristics of Sc-based double halide perovskites $K_2ScAgZ_6$ (Z= Cl, Br, I) for solar cells applications, *J. Phys. Chem. Solids*, 2023, **174**, 111115.

50 S. Al-Qaisi, *et al.*, A comprehensive first-principles study on the physical properties of $Sr_2ScBiO_6$ for low-cost energy technologies, *Opt. Quantum Electron.*, 2023, **55**(11), 1015.

51 K. A. Parrey, *et al.*, Electronic structure, optical and transport properties of double perovskite $La_2NbMnO_6$: a theoretical understanding from DFT calculations, *J. Electron. Mater.*, 2018, **47**(7), 3615–3621.

52 T. Liu, *et al.*, Enhanced control of self-doping in halide perovskites for improved thermoelectric performance, *Nat. Commun.*, 2019, **10**(1), 5750.

53 G. Pizzi, D. Volja, B. Kozinsky, M. Fornari and N. Marzari, BoltzWann: A code for the evaluation of thermoelectric and electronic transport properties with a maximally-localized Wannier functions basis, *Comput. Phys. Commun.*, 2014, **185**(1), 422–429.

54 H.-S. Kim, Z. M. Gibbs, Y. Tang, H. Wang and G. J. Snyder, Characterization of Lorenz number with Seebeck coefficient measurement, *APL Mater.*, 2015, **3**(4), 041506.

55 M. A. Jehangir, *et al.*, Crystal Stability, Chemical Bonding, Optical and Thermoelectric Properties of $LaAgZnX_2$ ($X = P$, As) Through First Principles Study, *J. Inorg. Organomet. Polym. Mater.*, 2024, **34**(8), 3769–3785.

56 Y. Lin, Y. Jia, G. Alva and G. Fang, Review on thermal conductivity enhancement, thermal properties and applications of phase change materials in thermal energy storage, *Renewable Sustainable Energy Rev.*, 2018, **82**, 2730–2742.

57 K. M. Wong, W. Khan, M. Shoaib, U. Shah, S. H. Khan and G. Murtaza, Ab initio investigation of the structural, electronic and optical properties of the $Li_2In_2XY_6$ ($X = Si$, Ge; Y= S, Se) compounds, *J. Electron. Mater.*, 2018, **47**(1), 566–576.

58 S. Naz, N. Israr, A. M. Tighezza, S. Khan, S. H. Shah and G. Murtaza, Pnictogen-based zintl Compounds: Unlocking the electronic, optical, and thermoelectric potential of $Mg_2ZnX_2$ ($X = P$, as, sb), *J. Phys. Chem. Solids*, 2025, **205**, 112805.

59 X. Yang, Y. Han, P. Xu and F. Liu, Thermodynamic stability descriptor of $A_2BX_6$-type perovskite materials, *Mater. Chem. Phys.*, 2025, **333**, 130324.

60 M. A. Jehangir, *et al.*, Exploring the stability, optoelectronic, and thermoelectric properties of Sc-based double perovskites $X_2ScAgI_6$ ($X = K$, Rb, Cs) for renewable energy applications, *Comput. Condens. Matter*, 2025, **42**, e00988.

61 H. Khan, G. Murtaza, M. B. Shakir, M. Touqir, S. Mumtaz and M. M. Azzam, Computational investigation of thermodynamic, optoelectronic and thermoelectric aspects of double perovskites $A_2YBiO_6$ ($A = Mg$, Ca, Ba): Promising green energy alternatives, *Chem. Phys. Lett.*, 2025, **868**, 142057.